

Interfacial Engineering of Porous Poly(p-Aminoazobenzene) toward Stable Zn Anodes

Xia Li, Ying Liu, Liangdan Chen, Long Su, Fei Lu, Hui Gu,* and Xinpei Gao*

Aqueous zinc-ion batteries (AZIBs) have recently emerged as a promising candidate for large-scale energy storage applications, primarily due to their nonflammable nature, low production costs, and satisfactory specific energy. Nevertheless, their cycle stability is significantly limited by the inevitable formation of Zn dendrites and undesirable water-induced parasitic reactions. To tackle these challenges, a porous poly(p-aminoazobenzene) (PPAAB) interfacial protective layer is developed for regulating the transport and deposition behavior of Zn^{2+} ions. The engineered PPAAB coating, functionalized with polar moieties ($-NH-$ and $=N-$), exhibits strong hydrophilic characteristics that

enable controlled Zn^{2+} ion flux and deposition behavior via a selective ion-confinement mechanism. Consequently, the $Zn@PPAAB$ anode exhibits improved interfacial dynamics and a low nucleation overpotential, demonstrating stable plating/stripping behavior. When paired with a NaV_3O_8 (NVO) cathode, the $NVO||PPAAB@Zn$ cell showcases impressive capacity retention, maintaining 84% of its capacity after 1100 cycles at 1.0 A g^{-1} . This study not only advances accessible interface engineering but also provides deeper mechanistic insights into Zn anode behavior, paving the way for enhanced AZIBs.

1. Introduction

Aqueous zinc-ion batteries (AZIBs) gained attention as a promising option for efficient energy storage systems, attributed to their inherent safety and cost advantages. Zn metal, with its high density of 7.14 g cm^{-3} and impressive theoretical capacity (820 mAh g^{-1}), stands out as a highly favorable anode material.^[1–5] Despite their potential, these critical issues, such as uncontrolled dendrite growth, harmful parasitic reactions, and corrosion of Zn anodes, significantly reduce coulombic efficiency (CE) and the battery's cycling lifespan.^[6–9] To address these challenges faced by Zn anodes and extend the lifetime of AZIBs, multiple strategies were proposed, including incorporating electrolyte additives to inhibit side reactions,^[10,11] developing advanced cathode materials to improve capacity,^[12] engineering functionalized separators to enhance tolerance,^[13] and constructing protective layers on the anode to prevent reactions with the electrolyte while providing abundant active sites.^[14–16]

Among the various strategies, constructing protective layers on the anode surface emerged as a particularly promising

approach to physically isolate the metal anode from reactive aqueous electrolytes.^[17–20] Central to its effectiveness is the attenuation of parasitic water activity at the electrode/electrolyte interface, where polar water molecules spontaneously adsorb onto the Zn anode within the inner Helmholtz plane and undergo interfacial decomposition, triggering hydrogen evolution and corrosion.^[21,22] By applying an artificial interfacial layer via non-in situ coating techniques, direct contact between Zn and the electrolyte was eliminated, thereby guiding uniform Zn deposition behavior and effectively protecting the Zn anode from water-induced side reactions and dendrite formation.^[23] To date, various coatings have been applied, including metallic coatings (such as Au,^[24] Ag,^[25] and In^[26]), non-metallic carbon-based modification layers (such as graphene oxide^[27]), and non-conductive layers (such as $CaCO_3$,^[28] ZnF_2 ^[29]). Nevertheless, the practical implementation of such inorganic interfacial coatings faces significant challenges due to their inherent low electrical conductivity and restricted active surface area. These material limitations impair homogeneous Zn^{2+} distribution and slow charge transfer kinetics, making it difficult to engineer artificial interphases capable of enabling truly reversible and stable Zn anode operation.

Organic polymers with polar groups offered abundant adsorption sites that can regulate the homogeneous distribution of Zn^{2+} through rapid ion transport. For instance, Cui et al. stabilized Zn anodes using a polyamide (PA) layer, where its hydrogen bonding network and strong Zn^{2+} coordination capacity synergistically facilitated ion migration, uniform nucleation, and water activity suppression.^[30] Similarly, Li et al. demonstrated that applying a nonconductive polyacrylamide (PAM)/polyvinylpyrrolidone (PVP) coating to the Zn anode effectively mitigated Zn dendrite growth and unwanted side reactions. Most importantly, PAM/PVP coating possessed polar groups ($C=O$ and $N-H$) that provided abundant adsorption sites to prevent Zn^{2+}

X. Li, L. Chen, L. Su, F. Lu, H. Gu, X. Gao
School of Chemistry and Chemical Engineering
Hainan University
Haikou 570228, P. R. China
E-mail: guh@hainanu.edu.cn
xpgao@hainanu.edu.cn

Y. Liu
Multi-scale Porous Materials Center
Institute of Advanced Interdisciplinary Studies
School of Chemistry and Chemical Engineering
Chongqing University
Chongqing 400044, P. R. China

 Supporting information for this article is available on the WWW under <https://doi.org/10.1002/batt.202500697>

accumulation at the tip, thereby promoting more uniform Zn deposition.^[31] These findings collectively establish that organic non-conductive coatings, enriched with polar functional groups, offer numerous sites for Zn²⁺ adsorption and facilitate the migration of Zn²⁺ along the mesoporous polymer pores toward the reaction interface. Additionally, these organic nonconductive coatings could act as electrostatic shielding layers to prevent the aggregation of Zn²⁺, thereby eliminating the “tip effect” and promoting uniform Zn deposition.^[32] However, the influence of the polar functional group content on performance has not been thoroughly investigated, which hinders the rational design of organic protective layers for enhanced AZIB performance.

Herein, polyaniline (PANI) and poly(p-aminoazobenzene) (PPAAB), both rich in polar functional groups (—NH— and =N—), were introduced as protective layers to physically separate the metal surface from the aqueous electrolyte, thereby suppressing corrosion and preventing dendrite formation (Figure 1a).^[33] Benefiting from the high density of its hydrophilic functional groups (—NH— and =N—) and small average pore size, the PPAAB layer facilitates the desolvation of hydrated Zn²⁺ ions and substantially enhances interfacial ionic mobility. Its tighter pore network also more effectively limits direct contact between the electrolyte and the Zn anode, suppressing parasitic water-induced side reactions (Figure 1b,c). As a result, Zn electrodes coated with PPAAB exhibit superior reversibility during plating and stripping and enhanced long-term cycling stability compared with those coated with PANI, highlighting the critical role of polymer microstructure in protective layer performance.

2. Results and Discussion

To investigate the effect of interfacial engineering on Zn anode stability, two organic polymers with differing functional group content were selected as protective layers. PANI and PPAAB were synthesized for this purpose, and their preparation routes are detailed in Figure S1, Supporting Information. Fourier transform infrared (FTIR) spectroscopy initially confirmed the successful preparation of PANI and PPAAB (Figure S2, S3, Supporting Information). The PANI spectrum (Table S1, Supporting Information) exhibited characteristic absorption bands at 3231 (N—H stretching), 1572 (C=N stretching), 1305 (C—N stretching in Q and B), 1123 (C=N + H—B and B—N + H—B stretching), and 800 cm⁻¹ (C—H stretching), consistent with previously reported data on PANI.^[34,35] The PPAAB spectrum exhibited a strong peak at 1507 cm⁻¹, attributed to C=C stretching vibration in a phenazine-like segment, a feature common to aniline-based oxidation products. Additionally, peaks at 1591, 1146, and 1460 cm⁻¹ correspond to 1,4-disubstituted rings and B—NH—B and N=N stretching vibrations, respectively (Table S2, Supporting Information).^[36] Further morphological analysis by field-emission scanning electron microscopy (FESEM) revealed that PPAAB possesses smaller and more densely distributed pores than PANI, suggesting improved structural integrity (Figure S4, Supporting Information).^[37,38] Consequently, Brunauer–Emmett–Teller (BET) analysis measured a higher specific surface area for PPAAB (25.5 m² g⁻¹) compared to PANI (20.72 m² g⁻¹) (Figure S5, Supporting Information). The increased surface area was expected to provide more active sites for adsorption and ion transport.^[14,39,40]

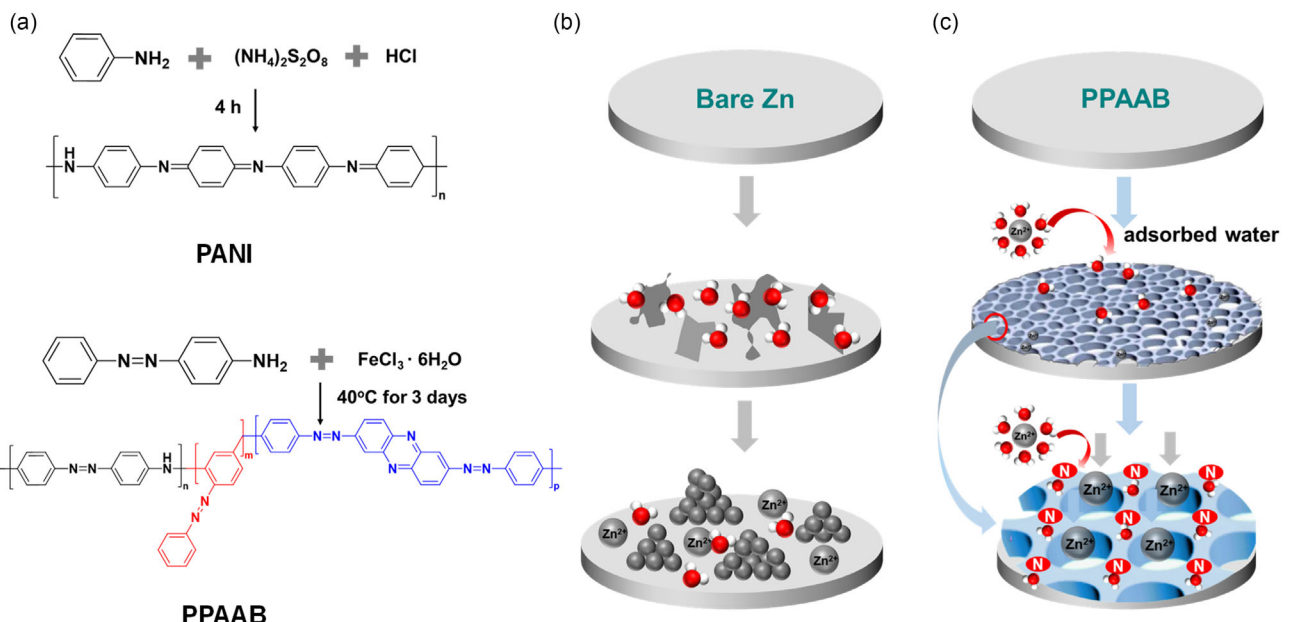


Figure 1. a) Schematic illustration of the structures of PANI and PPAAB, as well as Zn deposition process on b) bare Zn and c) the PPAAB modified Zn anodes.

The binding energies between H_2O and the $-\text{N}^+-$, $-\text{N}=$, and $-\text{NH}-$ groups were individually calculated using density functional theory (DFT), as shown in Figure S6, Supporting Information. The results showed that the binding energies of H_2O with the $-\text{N}=$ and $-\text{NH}-$ groups are negative, whereas the binding energy with the $-\text{N}^+-$ group is positive. This indicated that the $-\text{N}=$ and $-\text{NH}-$ groups exhibit strong hydrophilicity. Simultaneously, as shown in Figure 2a,b, DFT calculations revealed the desolvation of hydrated Zn^{2+} ($[\text{Zn}(\text{H}_2\text{O})_6]^{2+}$) on PANI and PPAAB layers. The adsorption energies for H_2O in PANI and PPAAB were -4.69 and $-5.58 \text{ kcal mol}^{-1}$, respectively. This stronger binding energy of PPAAB, which stemmed from its unique molecular structure, enabled it to modulate coordinated H_2O ligands, thereby facilitating Zn^{2+} desolvation and suppressing water-related side reactions.^[32]

To prepare polymer-modified Zn anodes, polymer powders were dispersed to form a slurry, which was then uniformly coated onto Zn foil surfaces using a coating device, as shown in Figure S7, Supporting Information. Further characterization by atomic force microscopy (AFM) revealed that the coating thicknesses were $3.1 \mu\text{m}$ for PANI and $3.8 \mu\text{m}$ for PPAAB, respectively (Figure S8, Supporting Information). X-ray photoelectron spectroscopy (XPS) analysis provided detailed insights into the chemical composition and bonding structures of PANI@Zn and PPAAB@Zn (Figure S9a, S10a, Supporting Information). The high-resolution C 1s spectrum of both polymers (Figure S9b, S10b, Supporting Information) exhibited distinct binding energies at 284.8 eV (C—H), 285.9 eV (C—N), and 286.8 eV (C=O). The Zn 2p XPS spectrum, as shown in Figure S9c, S10c, Supporting Information, exhibited two distinct peaks at ≈ 1022

and 1045 eV , which corresponded to the Zn $2p_{3/2}$ and Zn $2p_{1/2}$ states, respectively.^[41] The N 1s spectrum (Figure S9d, Supporting Information) revealed peaks at 398.6 and 399.8 eV corresponding to $=\text{N}-$ and $-\text{NH}-$ bond in PANI, respectively, while peaks at 400.5 and 402.7 eV were assigned to positively charged imine (bipolaron state) and protonated amine (polaron state), respectively.^[37,42] Similarly, the N 1s spectrum of PPAAB (Figure S10d, Supporting Information) showed distinct signals at 398.6 ($=\text{N}-$), 399.7 ($-\text{NH}-$), 400.1 ($-\text{N}=\text{N}-$), and 402.6 eV ($-\text{N}^+-$), which were characteristic peaks of PPAAB.^[38] Furthermore, the absolute nitrogen content, as determined by XPS (PPAAB: 18.88% , PANI: 9.34%) (Table S3, Supporting Information), confirmed a greater nitrogen presence in PPAAB. It was noteworthy that PPAAB (75%) possesses a higher content of polar functional groups ($-\text{NH}-$ and $=\text{N}-$) compared to PANI (53%), as evidenced by the results shown in Figure S11, Supporting Information. Taken together, these results indicated that PPAAB exhibits enhanced water affinity, which could be attributed to its higher concentration of $-\text{NH}-$ and $=\text{N}-$ functional groups on the polymer surface, thereby effectively suppressing the occurrence of side reactions in AZIBs.

Given that electrode wettability plays a critical role in influencing Zn deposition kinetics and the uniformity of electric field distribution, contact angle measurements were performed to assess the hydrophilicity of the PANI@Zn and PPAAB@Zn electrodes. Figure 2c showed the PPAAB@Zn electrode exhibited markedly improved wettability toward $2 \text{ M } \text{ZnSO}_4$ electrolyte, as evidenced by a contact angle of $55.5 \pm 2.1^\circ$, compared to $82.9 \pm 2.0^\circ$ for PANI@Zn and $97.2 \pm 2.3^\circ$ for bare Zn. This enhanced wettability was likely attributable to the increased

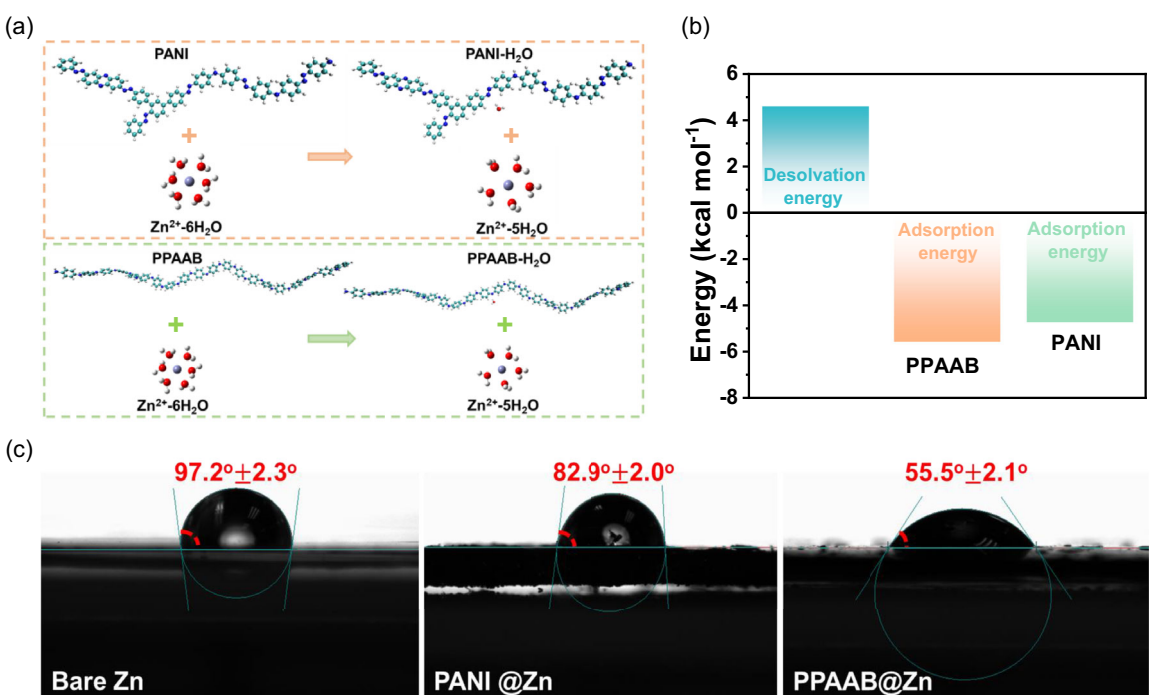


Figure 2. a) DFT of PANI and PPAAB adsorption of H_2O . b) The calculations of the H_2O adsorption energy of the $-\text{NH}-$ and $=\text{N}-$. c) Contact angle images of bare Zn, PANI@Zn, and PPAAB@Zn.

adsorption of water molecules by the more abundant polar functional groups present in PPAAB. Such properties would not only suppress water-induced side reactions but also improve the electrochemical stability of the electrode interface.

Collectively, these analyses established the superior physicochemical properties of PPAAB, including a higher density of polar functional groups, stronger H₂O adsorption energy, enhanced hydrophilicity, and a larger specific surface area with smaller pore size. These advantageous physicochemical properties would be expected to translate to enhanced interfacial kinetics, as demonstrated by cyclic voltammetry (CV) evaluation of Zn²⁺ stripping/plating behavior (Figure 3a–c). In the first cycle, the bare Zn and PANI electrodes exhibited oxidation peak potentials at −0.749 and −0.755 V, respectively. With successive cycling, a pronounced increase in the intensity of the oxidation peak was observed. Notably, the oxidation peaks for bare Zn and

PANI@Zn shifted positively from −0.749 and −0.755 V in the initial cycle to −0.737 and −0.745 V by the third cycle, respectively. This progressive shift and peak intensification are likely attributable to the emergence of side reactions, reflecting the instability of the cycling process. In contrast, the PPAAB@Zn half-cell displayed initial oxidation peaks at −0.714 V, with negligible changes in peak intensity after the third cycle, underscoring the superior cycling stability imparted by the PPAAB layer. Furthermore, a slight negative shift (−0.726 V) in the oxidation peak was detected, indicative of a reduced potential gap between oxidation and reduction peaks, thereby highlighting the beneficial effect of the PPAAB layer on electrochemical reversibility.^[43,44]

Electrochemical impedance spectroscopy (EIS) revealed distinct differences (Figure 3d). PPAAB@Zn exhibited the lowest impedance value (600 Ω) compared to bare Zn (1100 Ω) and

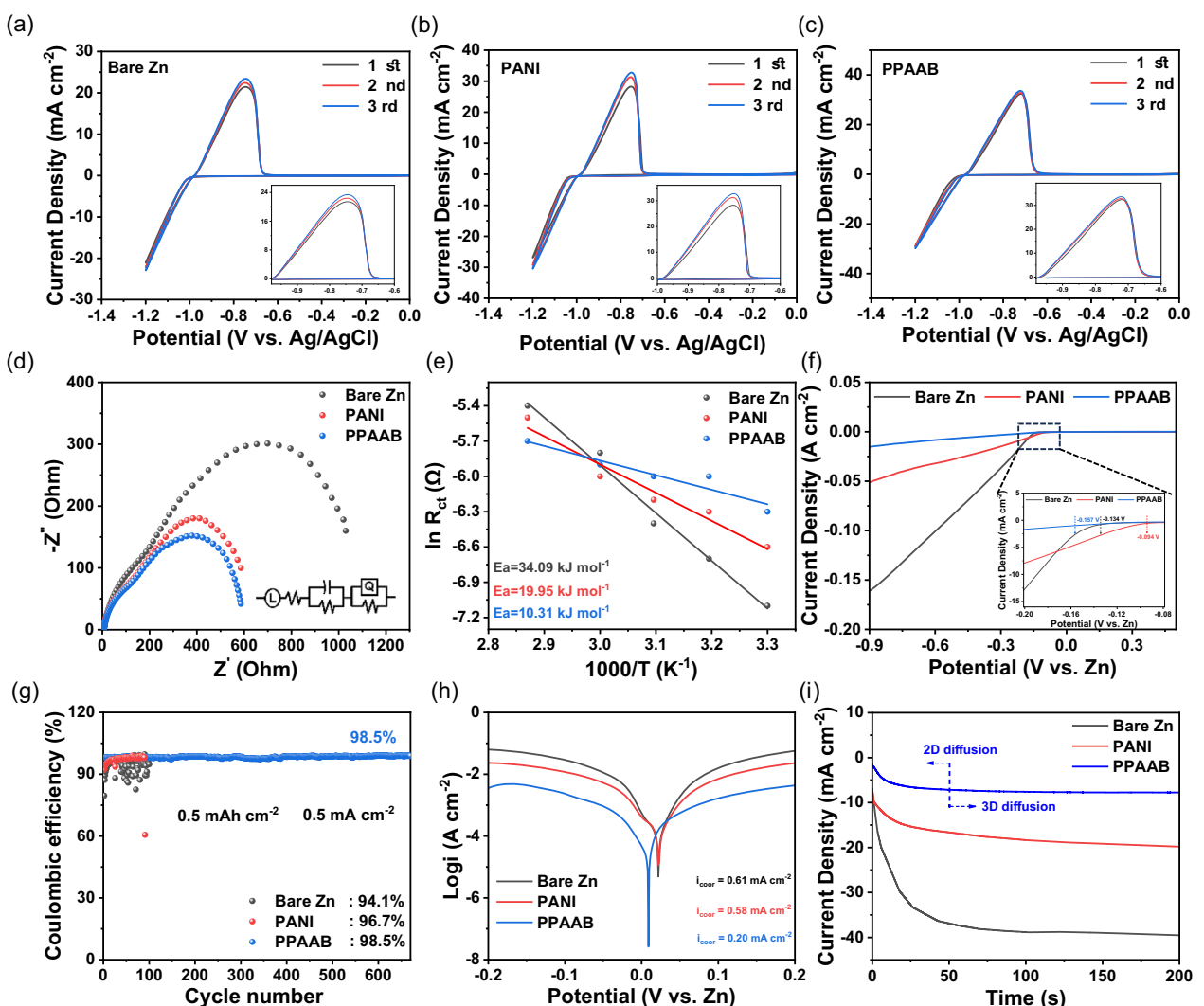


Figure 3. a–c) CV curves for bare Zn, PANI@Zn, and PPAAB@Zn electrodes. Three electrodes: Ag/AgCl reference electrode, Zn working electrode, and Cu counter electrode. d) Nyquist plots for bare Zn, PANI@Zn, and PPAAB@Zn anode. e) Ea calculations were based on the fitting of the Arrhenius curves. f) LSV curves of bare Zn, PANI@Zn, and PPAAB@Zn anode in 2 M ZnSO₄ aqueous solution with a scanning rate of 5 mV s^{−1}. g) CE of Zn||PANI@Cu, Zn||PPAAB@Cu, and Zn||Cu half cells at 0.5 with 0.5 mAh cm^{−2}. h) Tafel curve of a Zn||Ti cell with bare Zn, PANI@Zn, and PPAAB@Zn anode. i) Chronoamperometric curves of bare Zn, PANI@Zn, and PPAAB@Zn negative at an overpotential of −200 mV.

PANI@Zn ($650\ \Omega$), confirming its superior charge transfer kinetics during Zn deposition and dissolution cycles. This enhanced kinetics was further quantified by calculating the activation energy (E_a) for Zn^{2+} desolvation using the Arrhenius equation $k = A * e^{-E_a/(RT)}$ ^[45] and EIS data across temperatures (Figure S12, Supporting Information). PPAAB@Zn exhibited the lowest E_a ($10.31\ kJ\ mol^{-1}$), less than both bare Zn ($34.09\ kJ\ mol^{-1}$) and PANI@Zn ($19.95\ kJ\ mol^{-1}$) (Figure 3e). This reduced energy barrier, attributed to the abundant polar functional groups in the PPAAB layer that interact with H_2O , facilitates efficient desolvation and promotes uniform Zn^{2+} deposition. Consistent with the lowered energy barrier, nucleation overpotential measurements at $0.5\ mA\ cm^{-2}$ (Figure S13, Supporting Information) showed PPAAB@Zn required the lowest potential ($42.6\ mV$) to initiate Zn nucleation, which is markedly lower than bare Zn ($65.7\ mV$) and PANI@Zn ($59.8\ mV$).^[46]

The hydrogen evolution reaction (HER) presents a detrimental effect in Zn-based batteries, as this parasitic side reaction during metal deposition could generate gaseous products that might compromise cell integrity through pressure buildup.^[47] To evaluate the HER suppression capability of different polymer coatings, linear sweep voltammetry (LSV) measurements were performed. The results revealed distinct differences in HER onset potentials at the same cut-off current, with PPAAB-modified electrodes showed the most positive performance (Figure 3f). Specifically, the PPAAB@Zn system required $-0.157\ V$ to initiate hydrogen evolution, representing a $23\ mV$ improvement over bare Zn ($-0.134\ V$) and a substantial $63\ mV$ enhancement compared to PANI@Zn ($-0.094\ V$). The higher overpotential indicated that a greater voltage was required to initiate HER, suggesting that the PPAAB coating effectively inhibited HER at the Zn electrode.

To further assess the long-term reversibility of the Zn anode, the Zn plating/stripping CE was measured using $Zn||Cu$ half-cells at a current density of $0.5\ mA\ cm^{-2}$ with a capacity of $0.5\ mAh\ cm^{-2}$ (Figure 3g). Bare $Zn||Cu$ cell failed by cycle 50th, while PANI@Zn showed significant CE fluctuations after ≈ 100 cycles. In stark contrast, PPAAB@Zn maintained exceptional cycling stability with a high average (98.5%) over 650 cycles, underscoring its effectiveness in stabilizing Zn plating/stripping. Tafel curves were plotted to evaluate the protective capability of the coating on the Zn anodes (Figure 3h). The corrosion current was indicative of the corrosion rate, with a lower current density signifying a slower corrosion rate. The PPAAB@Zn electrode exhibited the lowest corrosion current density ($0.61\ mA\ cm^{-2}$ for bare Zn, $0.58\ mA\ cm^{-2}$ for PANI@Zn, and $0.20\ mA\ cm^{-2}$ for PPAAB@Zn), suggesting that the PPAAB layer acted as a significant barrier against corrosion. This barrier effectively prevented straightforward interaction between the Zn surface and the electrolyte, consequently minimizing the incidence of undesired secondary reactions.

Mechanistic insight into Zn deposition was gained through chronoamperometry (CA) on $Zn||Zn$ symmetric cells (Figure 3i). For the bare Zn and PANI@Zn symmetric cells, the current continued to increase over 100 and 200 s, respectively, and indicated 2D planar diffusion of Zn^{2+} on the anode surface. In contrast, Zn showed a unique deposition behavior in the PPAAB@Zn

symmetric cell. 2D planar diffusion and nucleation were carried out within 50 s, after which the system transitioned to a stable 3D diffusion process. This transition suggested that the PPAAB layer effectively inhibited prolonged 2D diffusion of Zn^{2+} , promoted uniform nucleation, and facilitated a more stable and uniform 3D Zn deposition. These results highlighted that the PPAAB layer likely promoted smoother Zn deposition by providing a uniform and conducive surface for Zn nucleation, thereby reducing localized deposition and suppressing dendrite growth.

Building on the favorable interfacial properties of PPAAB@Zn, namely reduced charge-transfer resistance, a lower desolvation energy barrier, suppressed hydrogen evolution, and enhanced nucleation uniformity, its impact on overall cell polarization and stability was further evaluated in symmetrical cells. The long-term cycling stability of symmetrical cells provided compelling evidence for PPAAB's protective efficacy (Figure 4a, S14, Supporting Information). At a current density of $0.1\ mA\ cm^{-2}$ with $0.1\ mAh\ cm^{-2}$, the bare Zn cell exhibited poor stability and short-circuited after $\approx 260\ h$, likely due to dendrite formation and side reactions. Remarkably, the PPAAB@Zn cell achieved exceptional stability exceeding $1900\ h$ under the same conditions. At a high current density of $0.5\ mA\ cm^{-2}$ with $0.5\ mAh\ cm^{-2}$ and $1.0\ mA\ cm^{-2}$ with $1.0\ mAh\ cm^{-2}$, the PPAAB@Zn symmetric cells exhibited highly reversible and stable cycling of 930 and $420\ h$, respectively, significantly outperforming the unmodified Zn and PANI@Zn anode. This demonstrated the effectiveness of the PPAAB coating in enhancing the durability and reliability of Zn-based batteries. Additionally, a comparative analysis with similar studies, presented in Table S4, Supporting Information, underscored the competitive performance of PPAAB at elevated current densities.

The X-ray diffraction (XRD) results presented in Figure 4b provided critical evidence for Zn deposition that the presence of the PPAAB layer effectively inhibited the generation of byproducts on the Zn anode surface, ensuring a more stable electrode-electrolyte interface. After 100 cycles, the bare Zn anode exhibited distinct XRD peaks at 8.1° , 16.2° , and 24.4° , characteristic peaks of the byproduct $Zn_4(OH)_6SO_4 \cdot 5H_2O$, whereas PANI@Zn exhibited weak characteristic peaks.^[48] Notably, the PPAAB@Zn showed negligible diffraction peaks for the byproduct, indicating its effectiveness in inhibiting the side reaction. Furthermore, to further demonstrate the effectiveness of PPAAB, XRD analysis was conducted on the anodes from symmetric cells comprising bare Zn, PANI@Zn, and PPAAB@Zn after varying cycling durations (Figure S15, Supporting Information). The results indicated that the formation of byproducts on both the bare Zn and PANI@Zn electrodes increases with prolonged cycling. In contrast, within a defined cycling time range, no distinct by-product peaks were observed in the XRD patterns of the PPAAB@Zn electrode, indicating its superior resistance to by-product accumulation during cycling.

To observe the morphology of Zn deposition on bare Zn and polymer-coated Zn, scanning electron microscopy (SEM) analysis was conducted. Morphological characterization using SEM was performed on each electrode prior to cycling (Figure S16, Supporting Information). Comparative analysis revealed that

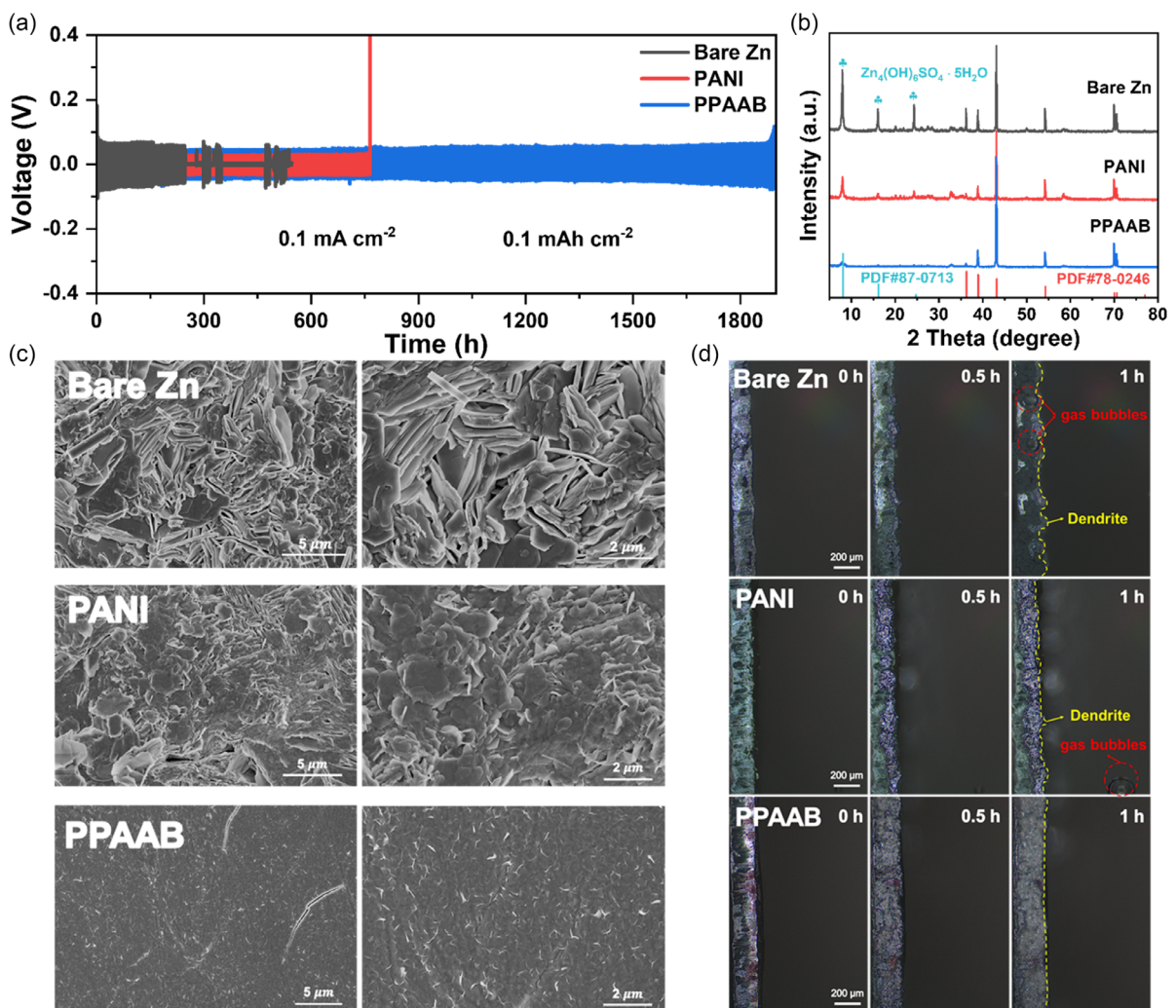


Figure 4. a) Galvanostatic cycling performance of $\text{Zn}||\text{Zn}$ cells at a density current of 0.1 mA cm^{-2} with 0.1 mAh cm^{-2} . b) XRD patterns of bare Zn, PANI@Zn, and PPAAB@Zn in symmetrical cells at 0.1 and 0.1 mAh cm^{-2} . SEM images of c) bare Zn, PANI@Zn, and PPAAB@Zn in symmetrical cells at 0.5 and 0.5 mAh cm^{-2} . d) In situ optical images of Zn deposition on bare Zn, PANI, and PPAAB at different times.

the surface of the PPAAB-modified electrode was markedly smoother than those of both the bare Zn and PANI@Zn electrodes. Elemental mapping was employed to elucidate the distribution of elements across bare Zn, PANI@Zn, and PPAAB@Zn electrodes following cycling. As illustrated in Figure S17, Supporting Information, the elemental distribution within the examined PPAAB@Zn region was notably uniform. Additionally, the by-products on PPAAB@Zn display a lower content of sulfur (S) and oxygen (O) compared to both bare Zn and PANI@Zn. This observation suggested that the PPAAB@Zn anode surface contains fewer by-products, which was consistent with the results obtained from XRD analysis. Furthermore, Figure 4c and Figure S18, Supporting Information, presented the surface morphology and cross-sectional views of Zn deposited on the different electrodes after 100 cycles, respectively, enabling direct comparison of their postcycling structural integrity. The surfaces of bare Zn and PANI@Zn electrode exhibited obvious agglomerations and protrusions, indicating the growth of dendrites.

In comparison, the PPAAB@Zn surface exhibited more uniform Zn deposition. This could be attributed to the high density of its hydrophilic functional groups ($-\text{NH}-$ and $=\text{N}-$). The PPAAB layer facilitates the desolvation of hydrated Zn^{2+} ions and substantially enhances interfacial ionic mobility, thereby resulting in a more uniform Zn deposition and stabilizing the Zn anode.

The Zn plating pattern was further observed using in situ optical microscopy at a current density of 3 mA cm^{-2} . As depicted in Figure 4d, Zn^{2+} deposited uniformly on the PPAAB-protected Zn anode to present a relatively smooth surface morphology without obvious gas evolution. In contrast, prominent dendrite formation and gas bubbles attributed to HER were evident on the surfaces of PANI@Zn and bare Zn. This distinct observation highlighted the efficient protection of the PPAAB layer, which significantly enhanced the stability of the Zn anode.

To further evaluate the practical feasibility of the PANI@Zn and PPAAB@Zn anodes, full cells were assembled with NaV_3O_8 (NVO) cathodes and a ZnSO_4 -based electrolyte. The reaction

kinetics of the PPAAB@Zn||NVO and PANI@Zn||NVO full cells were examined by CV at various scan rates (**Figure 5a**, S19a, Supporting Information). The CV curves exhibited a distinctive pair of redox peaks, which corresponded to the charge–discharge processes of the cells. To quantitatively understand the reaction kinetics, the relationship between the peak current (i) and the scan rate (v) could be analyzed using the power-law relationship, which followed the phenomenological model described by the equation:^[49,50] $i = av^b$, where the b value was a crucial parameter for determining the nature of the electrochemical reaction in the Zn||NVO full cell. Specifically, $b = 0.5$ indicated a diffusion-controlled process, where the reaction kinetics were dominated by the movement of ions through the electrode material or electrolyte, and $b = 1.0$ suggested a pseudocapacitive-controlled process, where the reaction kinetics were primarily governed by the surface-controlled process. As shown in Figure 5b, the fitting results revealed that the b -values of the PPAAB@Zn||NVO full cell were 0.71 and 0.68 for the charge and discharge processes, respectively. These values were notably higher than those observed for the PANI@Zn||NVO full cell (b -values of 0.65 and 0.64) (Figure S19b, Supporting Information). The higher b values for the PPAAB@Zn||NVO full cell suggested that its redox reaction

was predominantly dominated by pseudocapacitor-controlled behavior rather than diffusion limitations.^[49,51,52]

Rate capability tests were conducted at current densities ranging from 0.2 to 2 A g⁻¹, with active material loading maintained at ≈ 2.0 mg cm⁻² for all cells (Figure 5c). Specifically, the PPAAB@Zn||NVO full cell achieved a reversible discharge capacity of 281 mAh g⁻¹ at a current density of 0.2 A g⁻¹, which was significantly better than that of PANI@Zn||NVO (234 mAh g⁻¹) and Zn||NVO (178 mAh g⁻¹). Furthermore, the PPAAB@Zn full cell demonstrated exceptional capacity retention, highlighting its capability to preserve a significant portion of its initial capacity over extended cycles and under different charge/discharge conditions. Additionally, the long-term cycling data provided compelling evidence for the enhanced stability of PPAAB-modified full cells (Figure 5d). When cycled at 1 A g⁻¹, the NVO||PPAAB@Zn configuration maintained 192 mAh g⁻¹ after 1100 cycles, which represented an 84% retention of initial capacity. This performance substantially exceeded the capacity decay rates of 53% and 50% using unmodified Zn||NVO and PANI@Zn||NVO, respectively, under the same test conditions. As shown in Figure 5e–g, the slow capacity decay of PPAAB@Zn||NVO could be clearly observed. The above results indicated that the performance of

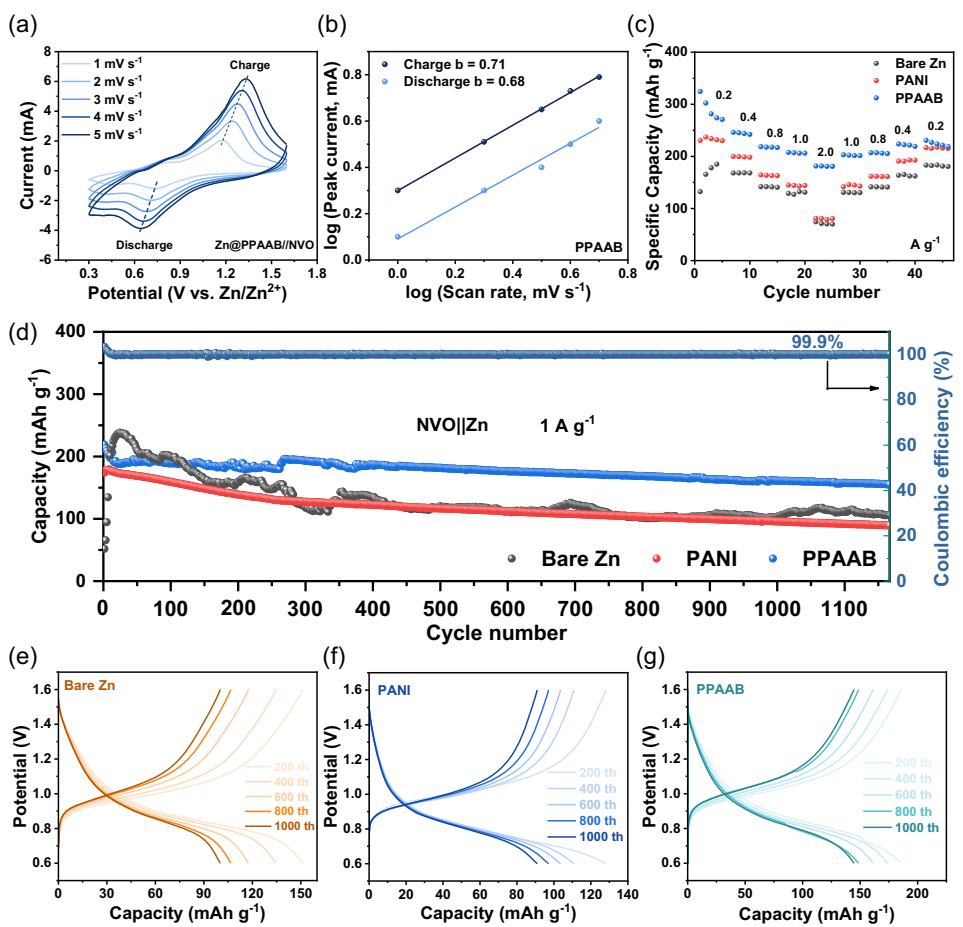


Figure 5. a) CV curves of PPAAB@Zn||NVO full cells at various scan rates. b) The corresponding b value of redox peaks. c) PPAAB@Zn||NVO, PANI@Zn||NVO, and Zn||NVO rate performance, as well as d) long-term cycling at 1 A g⁻¹ and e–g) corresponding voltage-capacity curves in different cycle numbers.

the PPAAB@Zn anode was significantly better than that of bare Zn and PANI@Zn, establishing its potential as a high performance and durable anode material for advanced aqueous Zn-based batteries.

3. Conclusion

In conclusion, a highly durable anode design was successfully developed by introducing a porous PPAAB protective layer for AZIBs. This interfacial layer effectively mitigated side reactions, lowered the corrosion rate, minimized voltage hysteresis, and reduced nucleation overpotential. As a result, it promoted faster diffusion and uniform deposition of Zn^{2+} ions. Additionally, the porous framework played a key role in homogenizing ion distribution, alleviating the issue of 2D irregular Zn^{2+} diffusion. The presence of hydrophilic functional groups ($-NH-$ and $=N-$) within the PPAAB layer enhanced overall performance by expediting the desolvation of hydrated Zn^{2+} ions. This mechanism effectively reduced detrimental interactions caused by reactive water molecules in the electrolyte, thereby improving electrochemical stability and efficiency. Most impressively, the assembled NVO||PPAAB@Zn full cell exhibited exceptional performance, achieving a specific capacity of 192 mAh g^{-1} while maintaining outstanding cycling stability, retaining 84% of its initial capacity after 1100 cycles at 1.0 A g^{-1} . This work underscored the importance of strategic interfacial design in realizing dendrite-free and compact anode structures, offering a promising pathway for the development of high-performance Zn-based batteries.

4. Experimental Section

Materials

Aniline hydrochloride ($C_6H_7N\cdot HCl$, AR), ammonium persulfate ($(NH_4)_2S_2O_8$), Iron(III) chloride hexahydrate ($FeCl_3\cdot 6H_2O$, AR), and p-aminoazobenzene hydrochloride (PAAB-HCl, AR) were purchased from Aladdin Chemical Reagent Company. Ethanol (C_2H_5OH , 95%), N-Nmethyl pyrrolidinone (NMP, AR), and ammonia ($NH_3\cdot H_2O$, AR) were purchased from Sinopharm Chemical Reagent Co., Ltd.

Synthesis of PANI

A solution containing 0.5 M $C_6H_7N\cdot HCl$ and 0.6 M $(NH_4)_2S_2O_8$ was blended, and ammonia was added. The mixture was subsequently stirred for a duration of 4 h and filtered through a sand core funnel. The filter cake was washed three times with methanol and dried in an oven at $60^\circ C$ to obtain PANI.^[32]

Synthesis of PPAAB

A mixed solution was obtained by dissolving 8.45 mM PAAB-HCl in a mixture of ethanol and deionized water. An aqueous solution of 14.07 mM $FeCl_3\cdot 6H_2O$ was slowly added dropwise to the above solution. The mixture was stirred at a constant temperature of $40^\circ C$ for 3 days. Afterwards, the resulting suspension was washed three times

with ethanol and deionized water, respectively, then treated with ammonia and left to stand overnight. PPAAB was dried in a vacuum oven at $60^\circ C$ to obtain PPAAB.^[36]

Electrochemical Measurements

To evaluate electrochemical performance under ambient conditions, a CR2032 button cell was assembled featuring a symmetric configuration. This configuration utilized modified Zn anodes paired with bare Zn flakes, separated by a glass fiber diaphragm. The 2 M $ZnSO_4$ solution was employed as the electrolyte to ensure efficient ion transport. The charge/discharge tests were conducted using a NEWARE battery test system to assess the electrochemical behavior. For the full cell setup, PANI@Zn and PPAAB@Zn were used as the anodes, while sodium vanadate ($NaV_3O_8\cdot 1.5H_2O$, NVO) served as the cathode. Preparation of cathodes: using a film applicator, the slurry was coated onto carbon cloth to fabricate the cathode. The slurry consisted of NVO nanosheets, Super P, and polyvinylidene fluoride (PVDF) in a weight ratio of 7:2:1, which were uniformly dispersed in N-methyl-2-pyrrolidone (NMP) to ensure thorough mixing.

Acknowledgements

This work was financially supported by the Natural Science Foundation of Hainan Province, China (224RC442). L.S., F.L., H.G., and X.G. acknowledge the Hainan University Scientific Research Startup Funds.

Conflict of Interest

The authors declare no conflict of interest.

Data Availability Statement

The data that support the findings of this study are available in the supplementary material of this article.

Keywords: deposition behavior • interfacial dynamics • interfacial protective layer • porous polymer • Zn anodes

- [1] L. E. Blanc, D. Kundu, L. F. Nazar, *Joule* **2020**, *4*, 771.
- [2] L. Chen, X. Li, X. Zhang, L. He, J. Li, F. Lu, H. Gu, L. Su, X. Gao, *Chem. Eng. Sci.* **2025**, *304*, 121080.
- [3] K. Kang, M. Cui, Z. Zhang, F. Jiang, *Batteries Supercaps* **2020**, *3*, 966.
- [4] C. He, Q. Jiang, Z. Yi, J. Yu, P. Li, S. Tan, J. Liang, *Batteries Supercaps* **2025**, *00*, e202500205.
- [5] D. Liu, X. Xu, S. Meng, J. Li, J. Feng, Y. Chen, W. Liu, F. Wu, W. Shi, X. Cao, *Batteries Supercaps* **2024**, *7*, e202400071.
- [6] X. Zhang, L. Zhang, X. Jia, W. Song, Y. Liu, *Nano Micro Lett.* **2024**, *16*, 75.
- [7] J. Liu, Z. Peng, R. Liao, J. Zhou, Q. Zhang, *Batteries Supercaps* **2025**, *00*, e202500420.
- [8] W. Lu, Y. Shao, R. Yan, Y. Zhang, J. Ning, Y. Hu, *Batteries Supercaps* **2024**, *7*, e202300486.
- [9] J. Jang, W. Lim, C. Jo, *Batteries Supercaps* **2024**, *7*, e202400365.
- [10] R. Qin, Y. Wang, M. Zhang, Y. Wang, S. Ding, A. Song, H. Yi, L. Yang, Y. Song, Y. Cui, J. Liu, Z. Wang, S. Li, Q. Zhao, F. Pan, *Nano Energy* **2021**, *80*, 105478.
- [11] Q. Zhang, Y. Ma, Y. Lu, Y. Ni, L. Lin, Z. Hao, Z. Yan, Q. Zhao, J. Chen, *J. Am. Chem. Soc.* **2022**, *144*, 18435.

- [12] W. Sun, F. Wang, S. Hou, C. Yang, X. Fan, Z. Ma, T. Gao, F. Han, R. Hu, M. Zhu, C. Wang, *J. Am. Chem. Soc.* **2017**, *139*, 9775.
- [13] L. Yao, C. Hou, M. Liu, H. Chen, Q. Zhao, Y. Zhao, Y. Wang, L. Liu, Z. Yin, J. Qiu, S. Li, R. Qin, F. Pan, *Adv. Funct. Mater.* **2023**, *33*, 2209301.
- [14] Z. Miao, F. Zhang, H. Zhao, M. Du, H. Li, H. Jiang, W. Li, Y. Sang, H. Liu, S. Wang, *Adv. Funct. Mater.* **2022**, *32*, 2111635.
- [15] X. Xie, S. Liang, J. Gao, S. Guo, J. Guo, C. Wang, G. Xu, X. Wu, G. Chen, J. Zhou, *Energy Environ. Sci.* **2020**, *13*, 503.
- [16] X. Li, Y. Chu, S. Lu, L. Chen, L. Su, F. Lu, Z. Chen, X. Gao, *Chem. Eng. J.* **2025**, *505*, 159182.
- [17] Y. Du, R. Li, T. Wang, Z. Feng, H. Dong, F. Fan, D. Deng, J. Zhu, Y. Liu, L. Dai, L. Wang, Z. He, *Chem. Eng. J.* **2024**, *486*, 150139.
- [18] Q. Sun, Y. Pang, H. Pan, W. Zhang, Z. Li, *Chem. Eng. J.* **2024**, *489*, 151296.
- [19] H. Q. Tian, S. Liu, L. J. Deng, L. Wang, L. Dai, *Energy Storage Mater.* **2021**, *39*, 232.
- [20] Q. Sun, S. H. Luo, Y. C. Lin, X. Yan, R. Huang, Q. Y. Liu, S. X. Yan, X. P. Lin, *Adv. Powder Mater.* **2025**, *4*, 100335.
- [21] Y. Niu, L. Chang, Y. Huang, Q. Sun, X. Lu, H. Cheng, *Chem. Eng. J.* **2024**, *499*, 155813.
- [22] Q. Luo, S. Xia, J. Liu, X. Yang, J. Lei, Y. Shi, X. Chen, J. Shao, X. Tang, G. Zhou, *Chem. Eng. J.* **2024**, *494*, 152789.
- [23] J. Yan, M. Ye, Y. Zhang, Y. Tang, C. C. Li, *Chem. Eng. J.* **2022**, *432*, 134227.
- [24] M. Cui, Y. Xiao, L. Kang, W. Du, Y. Gao, X. Sun, Y. Zhou, X. Li, H. Li, F. Jiang, C. Zhi, *ACS Appl. Energy Mater.* **2019**, *2*, 6490.
- [25] Q. Lu, C. Liu, Y. Du, X. Wang, L. Ding, A. Omar, D. Mikhailova, *ACS Appl. Mater. Interfaces* **2021**, *13*, 16869.
- [26] D. Han, S. Wu, S. Zhang, Y. Deng, C. Cui, L. Zhang, Y. Long, H. Li, Y. Tao, Z. Weng, Q. Yang, F. Kang, *Small* **2020**, *16*, 2001736.
- [27] A. Xia, X. Pu, Y. Tao, H. Liu, Y. Wang, *Appl. Surf. Sci.* **2019**, *481*, 852.
- [28] L. Kang, M. Cui, F. Jiang, Y. Gao, H. Luo, J. Liu, W. Liang, C. Zhi, *Adv. Energy Mater.* **2018**, *8*, 1801090.
- [29] J. Han, H. Euchner, M. Kuenzel, S. M. Hosseini, A. Groß, A. Varzi, S. Passerini, *ACS Energy Lett.* **2021**, *6*, 3063.
- [30] Z. Zhao, J. Zhao, Z. Hu, J. Li, J. Li, Y. Zhang, C. Wang, G. Cui, *Energy Environ. Sci.* **2019**, *12*, 1938.
- [31] Y. Li, J. Chen, P. Cai, Z. Wen, *J. Mater. Chem. A* **2018**, *6*, 4948.
- [32] B. Li, S. Liu, Y. Geng, C. Mao, L. Dai, L. Wang, S. C. Jun, B. Lu, Z. He, J. Zhou, *Adv. Funct. Mater.* **2024**, *34*, 2214033.
- [33] Q. Sun, S. H. Luo, Z. Z. Shi, X. Meng, J. Guo, S. X. Yan, *Chem. Eng. J.* **2025**, *521*, 166965.
- [34] J.-Z. Yen, Y.-C. Yang, H.-Y. Tuan, *Chem. Eng. J.* **2022**, *450*, 137924.
- [35] I. Karbownik, O. Rac-Rumijowska, M. Fiedot-Tobola, T. Rybicki, H. Teterycz, *Materials* **2019**, *12*, 664.
- [36] S. Shabzendedar, A. R. Modarresi-Alam, M. Noroozifar, H. Mansouri-Torshizi, *Synth. Met.* **2019**, *255*, 116115.
- [37] S. Golczak, A. Kanciurzecka, M. Fahlman, K. Langer, J. Langer, *Solid State Ionics* **2008**, *179*, 2234.
- [38] Z. Ai, L. Li, M. Huang, X. Su, Y. Gao, J. Wu, *Adv. Funct. Mater.* **2023**, *33*, 2211057.
- [39] W. Jian, W. Zhang, X. Wei, B. Wu, W. Liang, Y. Wu, J. Yin, K. Lu, Y. Chen, H. N. Alshareef, X. Qiu, *Adv. Funct. Mater.* **2022**, *32*, 2209914.
- [40] C. Zhao, Y. Lin, Q. Lin, Q. Liu, Y. Liu, Z. Liu, A. Ying, *Energy Storage Mater.* **2023**, *58*, 332.
- [41] I. G. Morozov, O. V. Belousova, D. Ortega, M.-K. Mafina, M. V. Kuznetcov, *J. Alloys Compd.* **2015**, *633*, 237.
- [42] F. Liu, S. Luo, D. Liu, W. Chen, Y. Huang, L. Dong, L. Wang, *ACS Appl. Mater. Interfaces* **2017**, *9*, 33791.
- [43] P. Liang, J. Yi, X. Liu, K. Wu, Z. Wang, J. Cui, Y. Liu, Y. Wang, Y. Xia, J. Zhang, *Adv. Funct. Mater.* **2020**, *30*, 1908528.
- [44] Y. Wang, H. Sun, N. Li, K. Chen, X. Yang, H. Liu, G. Zheng, J. Liu, Z. Wu, L. Zhai, L. Mi, *ACS Appl. Energy Mater.* **2022**, *5*, 2375.
- [45] D. Kundu, S. H. Vajargah, L. Wan, B. Adams, D. Prendergast, L. F. Nazar, *Energy Environ. Sci.* **2018**, *11*, 881.
- [46] Z. Miao, M. Du, H. Li, F. Zhang, H. Jiang, Y. Sang, Q. Li, H. Liu, S. Wang, *EcoMat* **2021**, *3*, e12125.
- [47] S. Zhang, J. Hao, D. Luo, P. Zhang, B. Zhang, K. Davey, Z. Lin, S. Qiao, *Adv. Energy Mater.* **2021**, *11*, 2102010.
- [48] X. Li, Y. Chu, S. Lu, L. Chen, L. Su, F. Lu, Z. Chen, X. Gao, *Chem. Eng. J.* **2025**, *505*, 159182.
- [49] L. Su, F. Lu, J. Dong, X. Dou, L. Zheng, C. Ouyang, X. Gao, *Adv. Energy Mater.* **2024**, *14*, 2400548.
- [50] L. Ma, M. A. Schroeder, O. Borodin, T. P. Pollard, M. S. Ding, C. Wang, K. Xu, *Nat. Energy* **2020**, *5*, 743.
- [51] Z. Tie, S. Deng, H. Cao, M. Yao, Z. Niu, J. Chen, *Angew. Chem., Int. Ed.* **2022**, *61*, e202115180.
- [52] X. Wang, X. Zhang, G. Zhao, H. Hong, Z. Tang, X. Xu, H. Li, C. Zhi, C. Han, *ACS Nano* **2022**, *16*, 6093.

Manuscript received: September 4, 2025

Revised manuscript received: October 9, 2025

Version of record online: